

## Photocatalytic CO<sub>2</sub> reduction with Graphene-based semiconductor

Zambaga Otgonbayar, Won-Chun Oh<sup>1\*</sup>

<sup>1</sup>Department of Advanced Materials Science & Engineering, Hanseo University, Chungnam, South Korea

---

**Abstract:** Photocatalytic carbon dioxide (CO<sub>2</sub>) reduction into hydrocarbon fuels over photocatalyst has theoretically and sensibly developed into a popular research topic. Nevertheless, the development of inexpensive, efficiently and exhibit high catalytic activity materials for the photocatalytic CO<sub>2</sub> reduction is challenging. The Graphene-based photocatalyst is showed a high catalytic activity due to large surface area, abundant active sites, enhance adsorption capacity, and a high electron-hole separation rate. The graphene is a 2D material owing to high conductivity, superior chemical stability and low cost, the outstanding point is providing a sufficient area for nanoparticle can growth on the surface of graphene. This article generally focuses on the recent important advances in the application of graphene-based photocatalyst for carbon dioxide (CO<sub>2</sub>) reduction to solar fuels.

**Keywords:** Graphene, Photocatalyst, semiconductor, Band gap energy, CO<sub>2</sub> reduction.

---

### Introduction

Fast growing scientific field provide an abundant and convenient energy resources to human society. In modern times, the most energy requirements are fulfilled by the combustion of fossil fuels. Fossil fuels is one of the largest sources of energy in the world, and their continuously combustion is among the primary contributor of carbon dioxide in the atmosphere. Currently, about 86% of the global energy needs is met through the combustion of oil, gas and coal [1]. There are several methods to use for carbon mitigation, such as thermal, electrochemical and photocatalytic reduction method. Photocatalytic reduction, which uses a semiconductor-based catalyst is ecologically the cheapest, safest and most environmentally friendly method. During the photocatalytic reduction, carbon dioxide and water are converted into hydrocarbon fuels such as CH<sub>4</sub>, HCO<sub>2</sub>H, CH<sub>2</sub>O, and CH<sub>3</sub>OH by utilizing solar energy and the final selectivity belonging to the photogenerated electrons and this characteristic has three important factors [2], [3], [4], [5], [6]. In addition, H<sub>2</sub>O acts as the essential proton donor during reduction process of CO<sub>2</sub> as a highest oxidation state of carbon, can be reduced into a variety of products Methanol (CH<sub>3</sub>OH) is the main product and the precursor to most industrial chemicals including formaldehyde, MTBE and acetic acid, which are used in adhesives, subfloors, solvents, washer fluids. Moreover, the production of methanol (CH<sub>3</sub>OH) is

more advantageous rather than CO and CH<sub>4</sub> as it is liquid at atmospheric temperature and pressure, making it desirable for energy storage [7]. In the field of photocatalytic reduction, to designing a well-structured catalyst is the main factor how carbon dioxide convert to carbon fuels. Specially, **semiconductor-based photocatalysis** has very essential and interesting field, because its potential applications in environmental purification, since the discovery of the Honda-Fujishima effect on water splitting for H<sub>2</sub> production over TiO<sub>2</sub> photoelectrodes in 1972 [8-10]. TiO<sub>2</sub>, as a typical (n-type) semiconductor has been regularly used for photocatalytic CO<sub>2</sub> reduction study, another one, can only assimilate UV-light (UVA, 315–400 nm, UVB, 280–315 nm, and UVC, 180–280 nm) because of its large bandgap [11, 12] (2.8 - 3.2 eV) which leads to low photocatalytic performance [13–14]. Graphene is one member of the carbon material and prepared by Hummer Offeman's method. The graphene (high electron mobility (250,000 cm<sup>2</sup>/ (V s) is increasing the surface area (oxygen functionality) of photocatalyst and promote the charge transfer. The outstanding point of graphene is a good candidate host material for **metal nanoparticles** to form nanocomposites because the oxygenated functional groups of graphene act as a stabilizer for metal nanoparticles and prevent their agglomeration. In addition, to prevent the recombination of photo-generated electron and holes, to activate the aggregation of photo-generated is the main factor for how to be designing the photocatalyst. Several researches studied to improve the photocatalytic activity semiconductor, including a noble metal deposition (e.g. Pt, Au, Pd, Ag) [15-19], non-metal doping (e.g. N, C) [20-23], surface sensitization [24, 25], coupling with narrow-bandgap semiconductors (e.g. CdS, g-C<sub>3</sub>N<sub>4</sub>, Cu<sub>2</sub>O) [26-31]. Semiconductor is a solid chemical element or compound that can conduct electricity under the proper condition, making a good medium for the control of electrical current. The conductance depends on the current or voltage applied to electrode (control), or on the intensity of irradiation by IR, Vis light, UV or X-rays. Typical of semiconductor:

- Stoichiometric: elemental, binary, tertiary, quaternary.
- Crystalline - small band gap materials semiconducting.
- Covalently bonded (mainly)

In a semiconductor, the current can be carried out by the flow of electrons or positively charged holes in the electron structure of the material. Depending on this semiconductor are classified into two categories: (i) Intrinsic- [pure semiconductor, it's the one where the number of holes are equal to the number of electrons], (ii) Extrinsic- [small amount of purity has been added into the intrinsic semiconductor]. Based on extrinsic semiconductor have two types:

- ✓ N-type semiconductor: the electrons are the majority charge carriers. A small amount of pentavalent impurity is added into a pure semiconductor and providing many free electrons.
- ✓ P-type semiconductor: the holes are the majority charge carriers. The fermi level is near the Valence band edge. A small amount of trivalent impurity is added into a pure semiconductor to create many holes.

In a solid-state physics, a range of energy levels within a given crystal that are impossible for an electron to possess, is called a "Bandgap". The band gap is major factor to determine the electrical conductivity of a solid. **Figure 1** expresses the electronic band structure of solid-state material; the band gap generally refers the energy difference between the top state and bottom state. Top state is a valence band which is completely filled, the bottom state is a conduction band is completely empty, then electron cannot move in the solid, however, if some electron can transfer from the valence band to the conduction band after that the current can flow. Depend on the band gap difference, solid-state material divided into three groups: (i) insulator-large band gap, (ii) semiconductor- smaller band gap, (iii) conductor- either have very small band gap or none, because the valence band and conduction band is overlapped and **Figure 2** expresses the band structure difference. The band gap of semiconductor has two types, a direct and indirect. The minimal-energy state in the conduction band and the maximal-energy state in the valence band are each characterized by a certain crystal momentum ( $k$ -vector) in the Brillouin zone. If the valence band maximum and the conduction band minimum have the same crystal momentum ( $k$ -vector) in the Brillouin zone, then the resultant optical transition is termed a "direct" transition [32] and expressed in **Figure 3**. On the other hand, an indirect bandgap material would have to have phonon coupling for the optical transition to occur. Examples of direct bandgap material include some III-V materials such as InAs, GaAs. Indirect bandgap materials include Si, Ge. Some III-V materials are indirect bandgap as well, for example AlSb. During our ongoing, collaborative efforts to screen new generations of oxide semiconductor candidates for solar fuels generation [33], [34], [35], wide variations were noted in the reported bandgap values in the literature for a given semiconductor, especially for ternary oxides. **Figure 4** shows a bandgap energy and structure for some oxide semiconductors. Photocatalysis, especially semiconductor based photocatalysis is a one of the promising methods to solve the environmental problems and energy crisis [36], [37]. Photocatalyst with low band gap energy is more profitable as it is easily exciting under the visible light. It is common to apply the top-down approach whereby dopant or catalyst pairing was introduced to the base wide bandgap material to form visible-responsive catalyst. The general mechanism of redox (reduction and oxidation) reaction with semiconductors as photocatalysts is shown in **Figure 5**. It consists of consecutive steps. Firstly, the electron in the valence band of the semiconductor is excited and migrated into conduction band with light assistance. Subsequently, the excited electrons and holes are transferred to the surface of the catalyst. Then the electron is consumed in the reduction reaction, while the hole which carries the positive charge, is used in the oxidation reaction. Depend on the structure and chemical nature of photocatalyst have three categories. Furthermore, the advantage of homogeneous (only p or n-type semiconductor, selectivity, tunability) and heterogeneous (p and n-type semiconductor co-operated with another semiconductor, robustness, easy separation of product) catalyst and p-n junction structured photocatalyst commonly used reduction of carbon dioxide. The **Table 1** presents the summarize data of photocatalytic material and experimental condition.

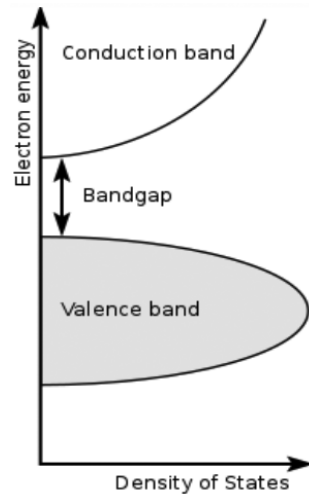


Figure 1. Semiconductor band structure.

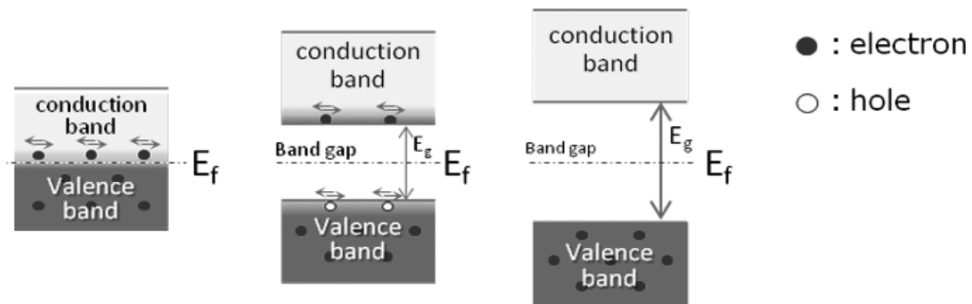


Figure 2. Band structure of solid-state material.

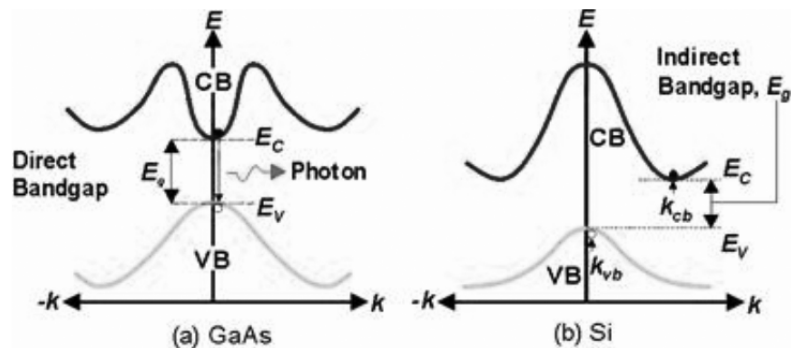


Figure 3. Indirect and direct band gap.

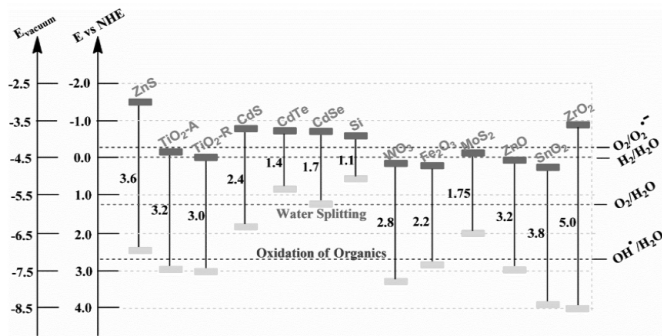


Figure 4. Variability of reported band gap ( $E_g$ ) values in the literature for the oxide (13) semiconductors.

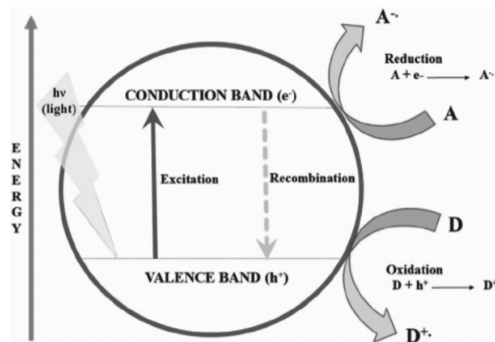


Figure 5. Mechanism of photocatalysis reactions driven by a semiconductor.

**Table 1. Photocatalyst categories for carbon dioxide reduction, light source type and experiment condition.**

Description	Irradiation type	Experimental condition	Example
			Inorganic
Single-metal oxides	UV/Vis	Solid gas (catalyst- $\text{CO}_2/\text{H}_2\text{O}$ ), systems/Aqueous dispersions	$\text{TiO}_2$ , $\text{WO}_3$ , $\text{ZnO}$ , $\text{Pb}_3\text{O}_4$ , $\text{BiO}$ , $\text{CeO}_2$
Mixed-metal oxides	UV/Vis	Solid-gas (catalyst- $\text{CO}_2/\text{H}_2\text{O}$ ) systems/Aqueous dispersions	$\text{BiVO}_4$ , $\text{Bi}_2\text{WO}_6$ , $\text{CaFe}_2\text{O}_4$ , $\text{LaCoO}_3$ , $\text{NaBiO}_3$ , $\text{NaNbO}_3$ , $\text{KNbO}_3$ , $\text{CuGaO}_2$ , $\text{CuAlGaO}_4$
Metal oxide composites	Vis	Solid-gas (catalyst- $\text{CO}_2/\text{H}_2\text{O}$ ) systems/Aqueous dispersions	$\text{NiO}/\text{InTaO}_4$ , $\text{Pt}$ (0.5%wt), $\text{ZnAl}_2\text{O}_4/\text{ZnGaNO}$ , $\text{CuO}/\text{ZnO}$ supported on $\text{MgO}$
Layer Double Hydroxides (LDHs)	UV/Vis	Solid-gas (catalyst- $\text{CO}_2/\text{H}_2\text{O}$ , catalyst- $\text{CO}_2/\text{H}_2$ ) systems/Aqueous dispersions	$\text{Zn-Cu-Ga}$ layered double hydroxide (LDH)
Carbonaceous			
Graphene (GR) based	Vis	Aqueous dispersions	$(\text{BiO})_2\text{CO}_3/\text{GR}$
Carbon nanotubes (CNTs) based	Vis	Aqueous dispersions	$\text{Ag}/\text{AgBr}/\text{CNT}$
$\text{g-C}_3\text{N}_4$ based	Vis	Aqueous dispersions/Solid-gas (catalyst- $\text{CO}_2/\text{H}_2\text{O}$ ) systems	$\text{WO}_3/\text{g-C}_3\text{N}_4$ composites
Hybrid organic-inorganic	Vis	Aqueous/organic solutions	Zeolithic imidazolate frameworks (ZIFs)

The main objective of in this study is to summarize the progress of the Graphene-based photocatalytic carbon dioxide reduction system. In addition, to sum up to the synthesis of new type of nanocomposite combined Graphene and the catalytic activity for photocatalytic carbon dioxide under the light irradiation

## Experimental method

### *Synthesis of Graphene*

Graphene is a 2-dimensional material of  $sp^2$  carbon atoms in a honeycomb structure. It has been shown to have many profitable properties, such as mechanical strength [38], electrical conductivity [39], molecular barrier abilities [40] and other remarkable properties. The synthesis method of graphene has divided into two groups: (i) top-down method (nanostructures are synthesized by etching out crystal planes), (ii) bottom-up method (nanostructures are synthesized by the atoms stacking onto the substrate which gives rise to crystal planes). The structure of Graphene oxide had several kinds, namely the Hofmann, Ruess, Scholz-Boehm, Nakajima-Matsuo, Lerf-Klinowski and Szabo models [41] as illustrated in **Table 2**.

**Table 2. Synthesis procedure of Graphene.**

	Top-down synthesis	Bottom-up synthesis	
Mechanical exfoliation -(cheapest method)	Quickest and most precise method of identifying the thickness of graphene flake and estimating its crystalline quality.	Chemical vapor deposition	High quality graphene with low defects, highly interconnected structure and large surface area.
Liquid-phase exfoliation.	(i) Disperse graphite in a suitable solvent, (ii) exfoliate and (iii) purify the final products.	Epitaxial growth	Thermal decomposition (1200-1600°C) of hexagonal substrate (silicon carbide (SiC)) under vacuum or inert condition.
Chemical exfoliation	First manufactured Brodie, Stauden- maier and Hummers (fast and safe process) methods.		

### *Synthesis of Graphene-semiconductor*

Combining semiconductor with graphene to form composite materials is expected to environmental pollution to a certain extent. Graphene is a basic unit in carbon atrial and compared with other carbon material, it's showing a high stability, conductivity and unique 2-dimensional planar structure to provide a high surface area. There are number of methods used for synthesis of graphene-semiconductor composites with diverse morphology, size, dimensionality and all affecting the efficiency of the photocatalytic process. All synthesis procedure divided into two groups: (i) In-situ crystallization, (ii) Ex-situ crystallization.

In-situ method is one of the simple and unique method, including a **sol-gel method**, **hydrothermal/solvothermal treatment**, and **microwave-assisted deposition** have been exploited to construct Graphene-based composites through a one-step growth or by a multistep reaction procedure. To sum up to basic knowledge of this method is, carbon material and

soluble precursor of the inorganic semiconductor in a solvent and treat with chemical, thermal, optical ultrasonic treatment, anchoring the surface of graphene. Ex-situ method is a unique method, including a **self-assembly method** have been utilized to construct a Graphene-based composites. To sum up to basic knowledge of this method is: anchor the inorganic particles to oxygen moieties existing on the surface of graphene via covalent or noncovalent interaction [49]. The advantage of ex-situ method is to control the morphology of the materials into ordered and monodisperse structures by pre-selection of semiconductors with desirable morphology. In the course of ex-situ preparations, the shape, size and morphology of the used semiconductors in the composites are nearly the same as the initial ones.

### *Overview of photocatalytic reduction methods*

Carbon dioxide ( $\text{CO}_2$ ) is a kinetically and thermodynamically stable molecule, thus  $\text{CO}_2$  conversion reactions are endothermic and need efficient catalysts to obtain high yield. The reduction of carbon dioxide consists of three major categories: (i) electrochemical, (ii) photo-electrochemical, (iii) photocatalytic. The first one, electrochemical carbon dioxide reduction (ERC) is using electrical energy for conversion of carbon dioxide to reduced chemical species. This reduction method is a proper approach to producing a hydrogen containing product, such as formic acid ( $\text{HCOOH}$ ), methanol ( $\text{CH}_3\text{OH}$ ), ethylene ( $\text{C}_2\text{H}_4$ ), methane ( $\text{CH}_4$ ), and carbon monoxide ( $\text{CO}$ ). The first examples of electrochemical reduction of carbon dioxide are from the 19th century, when carbon dioxide was reduced to carbon monoxide using a Zinc cathode. The second, photo-electrochemical carbon dioxide reduction is using a semiconductor-based electrode and supply with electric energy for conversion of carbon dioxide to final reduced product. In this study field, the band gap energy of semiconductor is the most important area. Aqueous and non-aqueous solvent have been used for photo-electrochemical carbon dioxide reduction on flat semiconductor surfaces, especially non-aqueous solvent condition being reported [42-45]. In the case of non-aqueous solvent, solubility of carbon dioxide is 7 to 8 times greater than water. Carbon dioxide solubility, maximum catalytic current and the pressure of carbon dioxide environment, in addition, proton reduction for metal and semiconductor electrode affect the reduction process. The third, photocatalytic carbon dioxide reduction is an effective approach towards solving the above problems and can utilize sustainable and environmentally friendly solar energy to convert  $\text{CO}_2$  into value-added chemicals, simultaneously reducing  $\text{CO}_2$  emissions and providing renewable energy. Since 1979, when Inoue et al. reported the first time for photocatalytic reduction of carbon dioxide [54], various photocatalysts, such as  $\text{TiO}_2$ ,  $\text{ZnO}$ , and  $\text{CeO}_2$  have been applied in photocatalytic  $\text{CO}_2$  reduction.

The experimental part of photocatalytic  $\text{CO}_2$  reduction was performed in a reactor (composed of three-part) for this design, as shown in **Scheme 1**. A cylindrical quartz reactor with 50/ mm height and 20/ mm inner diameter was equipped with gas inlet, outlet and a gas sampling port. High precision Mass Flow Controllers were used to control gas flow into the chamber from Nitrogen and  $\text{CO}_2$  cylinders. The gas mixture was passed through a water column kept at room temperature for carrying moisture. Precise amount of photocatalyst placed in the reactor.

To remove possible sources of contamination, the reactor was repeatedly flushed with Nitrogen (99.995%, Sigma gas) and finally water saturated CO<sub>2</sub> (99.999%, Sigma gas) was filled in after purging for 30 minutes [46]. The final product is a hydrogen and carbon-containing component, such as alcohols, aldehydes and acids. To analyze the form of the final product to use a blank experiment from correct photocatalytic carbon dioxide reduction. The blank experiment was performed under the following conditions: (a) filling up the chamber with water vapor mixed CO<sub>2</sub> but without sample and light irradiation (visible and UV light), (b) filling up the chamber as in (a) and shining light irradiation (visible and UV) but without sample, (c) filling up the chamber with moist CO<sub>2</sub> and catalyst sample but without light radiation and (d) fillip up the chamber with water vapor mixed N<sub>2</sub> in presence of both light and radiation (visible and UV). The photosynthetic reaction can be summarized into three processes; (1) generation of charge carriers or electron-hole pairs upon suitable light-harvesting, (2) charge carrier separation and transportation, and (3) catalytic reactions between surface species and charge carriers [47]. Photocatalytic carbon dioxide reduction with water over photocatalyst (TiO<sub>2</sub>) involves three main steps (**Figure 6**). First, carbon dioxide and water are adsorbed on the surface of photocatalyst. Second, the electrons excited from valence band to conduction band of photocatalyst, then produce a photogenerated electrons and holes pairs. Third, the excited electrons can migrate to the surface of photocatalyst and reduce the adsorbed carbon dioxide to form solar fuels (e.g., CO, CH<sub>4</sub>, CH<sub>3</sub>OH, and HCOOH), meanwhile, the photogenerated holes oxidize water to form oxygen and hydrogen. The efficiency of photocatalytic carbon dioxide reduction depends on the light source, charge separation and surface reaction capability. Specifically, the separation of photogenerated electron-hole pairs is a great factor in this process, because charge recombination rate (<"10<sup>-9</sup> s) is usually faster than the reduction process (<"10<sup>-3</sup><"10<sup>-8</sup> s). The original form of final product of hydrogen and carbon containing from photocatalytic carbon dioxide reduction with photocatalyst should desire two requirements: 1. the confirmation of carbon source of the carbon-containing products from carbon dioxide by using isotope labeling experiments, 2. the stoichiometric generation of O<sub>2</sub> from water oxidation. Some researchers carefully explored the carbon source of carbon-containing products generated during CO<sub>2</sub> photocatalytic reduction over TiO<sub>2</sub> photocatalysts by using isotopic <sup>13</sup>C-labeling experiments [48]. For example, Low et al. [49] performed a <sup>13</sup>CO<sub>2</sub> isotope analysis to confirm the carbon source of the CH<sub>4</sub> generated during gaseous CO<sub>2</sub> photoreduction over Ag loaded TiO<sub>2</sub> nanotube arrays. More conclusive evidence that the hydrocarbon products were formed from CO<sub>2</sub> photocatalytic reduction over TiO<sub>2</sub> photocatalysts was provided by Ohno et al [50]. They used <sup>1</sup>H-NMR spectroscopy to analyze the carbon source of products generated in the CO<sub>2</sub> photocatalytic reduction with water over Au loaded brookite TiO<sub>2</sub> nanorods with co-exposed {210} and {212} facets.

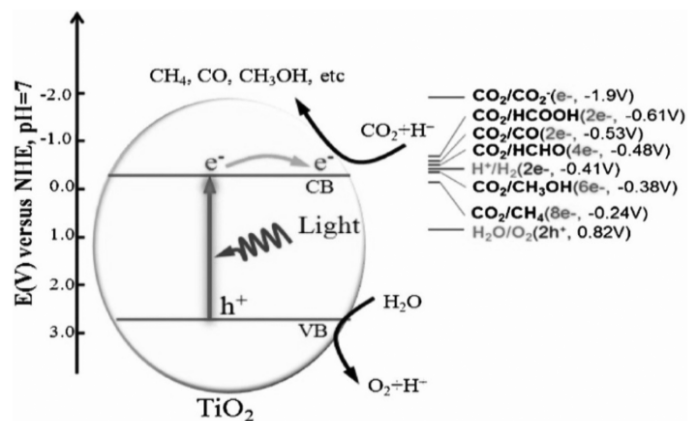
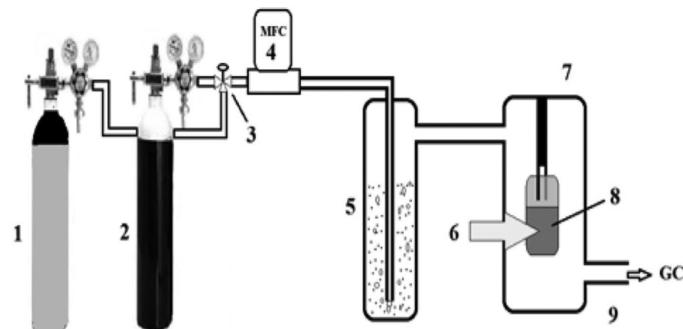


Figure 6. Schematic illustration of the mechanism of the photocatalytic reduction of  $\text{CO}_2$  with water over  $\text{TiO}_2$ .



Scheme 1. Schematic reaction set-up for photocatalytic reduction of  $\text{CO}_2$ . 1.  $\text{N}_2$  cylinder, 2.  $\text{CO}_2$  cylinder, 3. Three-way valve, 4. Mass flow controller, 5. Water saturator, 6. Optical fiber guided UV-A Light to focus at one side of catalyst coated plat, 7. Quartz reactor, 8. Catalyst coated titanium plate hanged at the centre of reactor, 9. Outlet for online GC injection for product analysis.

#### Computation of photocatalytic product

Photocatalytic carbon dioxide reduction can produce many type of product and the amount is generally low due to the conversion capability of raw material. Final product state has gas and liquid phase.  $\text{CO}$ ,  $\text{H}_2$ ,  $\text{O}_2$  and hydrocarbons (mainly  $\text{CH}_4$ ) are the main gaseous products of  $\text{CO}_2$  photoreduction with water. Gas chromatography (GC) is the main instrument for quantitative determination of gaseous products [51]. The GC is usually equipped with an FID, a TCD, and a methanizer. The different gas components in the samples are separated by columns first and analyzed by FID and TCD thereafter. The liquid phase products mainly include alcohols, aldehydes, and carboxylic acids. Gas chromatography/FID is the main analysis technique for the quantitative examine of alcohols and aldehydes [52]. The liquid phase oxygenates are usually dispersed in the

catalyst suspension, to analyze the liquid sample need to be filtered to remove the solid catalyst particles before inoculation into the GC. For the quantitative analysis of carboxylic acids, high performance liquid chromatography (HPLC) and ion exchange chromatography (IEC) were suggested [53-56]. Aldehydes can also be quantitative determined by HPLC after being derivate [57, 58]. NMR and GC/LC-MS can analyze all oxygenate but they are mainly used for the product qualification and carbon source verification [59].

## Result and discussion

### Characterization of synthesized sample

**Figure 7** shows the XRD pattern of all synthesized nanocomposite. XRD analysis was applied the crystal structure and phase composition of all the synthesized samples. Figure 7 (a) and (b) presents the XRD spectrum of pure  $\text{g-C}_3\text{N}_4$ , 0.5% CNTs/pCN, 3% Cu/pCN and 3wt % Cu-doped 0.5wt% CNT/pCN samples,  $\text{g-C}_3\text{N}_4$  foam, CFC-0.05, CFC-0.1, CFC-0.2 and CFC-0.4. The XRD spectrum of pure  $\text{g-C}_3\text{N}_4$  show two distinct diûraction peaks appeared at  $2\theta$  values of  $27.7^\circ$  and  $13.03^\circ$ . The XRD patterns of Cu and CNTs modified pCN samples show only  $\text{g-C}_3\text{N}_4$  peaks, however, typical diûraction peaks relating to Cu and CNTs were not appeared. The strong diûraction peak at  $27.7^\circ$  ascribes to (002) plane of carbon nitride, demonstrates typical graphitelike interlayer stacking of  $\text{C}_3\text{N}_4$ , as shown in Figure 7 (a). The  $\text{g-C}_3\text{N}_4$  foam/ $\text{Cu}_2\text{O}$  QDs composites gave the similar XRD peaks in comparison with pure  $\text{g-C}_3\text{N}_4$  foam. While a feeble XRD peak at  $36.4^\circ$  was observed for CFC-0.1, CFC0.2 and CFC-0.4, which is assigned to the (111) plane of the  $\text{Cu}_2\text{O}$  (JCPDS No. 05-0667), as shown in Figure 7 (b). In the case of pure  $\text{g-C}_3\text{N}_4$  foam, the strongest peak at  $27.41^\circ$  ( $d=0.326\text{nm}$ ) was a characteristic interlayer stacking peak of aromatic systems, indexed for graphitic materials as the (002) crystal plane.

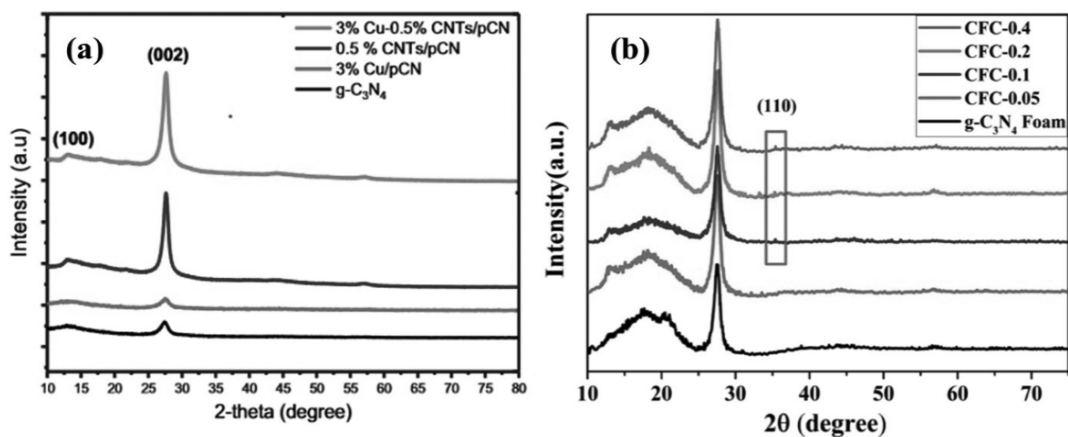


Figure 7. XRD pattern of (a) pure  $\text{g-C}_3\text{N}_4$ , 0.5% CNTs/pCN, 3% Cu/pCN and 3wt % Cu-doped 0.5wt% CNT/pCN samples, (b)  $\text{g-C}_3\text{N}_4$  foam, CFC-0.05, CFC-0.1, CFC-0.2 and CFC 0.4.

**Figure 8** expresses the TEM and HRTEM image of  $\text{g-C}_3\text{N}_4$  catalyst, 2D pCN, CNTs, Cu-loaded CNTs/pCN composite structure, which analyze the morphology and construction of nanocomposite. The morphology of pure  $\text{g-C}_3\text{N}_4$  is presented in Figure 8 (a), which reveals compacts sheets attached together. However, exfoliation and protonation process give thin sheets with 2D structure presented in Figure 8 (b). The interaction of CNTs with pCN is presented in Figure 8 (d-e). The further interaction of CNTs/pCN loaded with Cu was identified using HRTEM and the results and there is a good interaction between CNTs and pCN, while Cu is evenly distributed over the composite structure. **Figure 9** the microstructure of the obtained  $\text{g-C}_3\text{N}_4$  foam was constructed by well-arranged globular pores, the wall of the pore was formed by connecting  $\text{g-C}_3\text{N}_4$ . The size of the globular pores ranged from 30 to 90 nm, inheriting the morphology of the foam templates. The SEM images of  $\text{g-C}_3\text{N}_4$  foam/ $\text{Cu}_2\text{O}$  QDs composites, it is revealed that the three-dimensional porous structure was still preserved after depositing the  $\text{Cu}_2\text{O}$  QDs. In the result of TEM image, all composite samples well displayed the unique nanosheet structure with smooth outer surface of  $\text{g-C}_3\text{N}_4$ . Moreover, some dark nanoparticles can be found in all composite samples, the distribution of nanoparticles was uniform, and the dimension of the nanoparticles dispersed on the surface of  $\text{g-C}_3\text{N}_4$  foam can be gauged to be 5-10 nm.

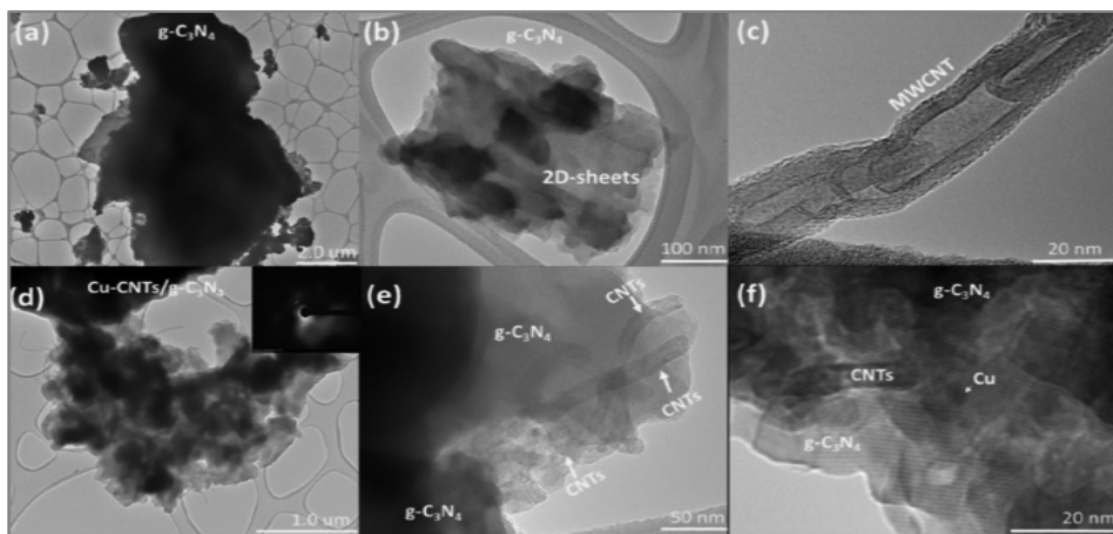


Figure 8. TEM analysis of Cu-modified CNTs/pCN samples: (a) TEM image of  $\text{g-C}_3\text{N}_4$  catalyst, (b) TEM images of 2D pCN sample; (c) Image of CNTs, (d-e) CNTs distributed in pCN, (f) HRTEM image presenting Cu-loaded CNTs/pCN composite structure.

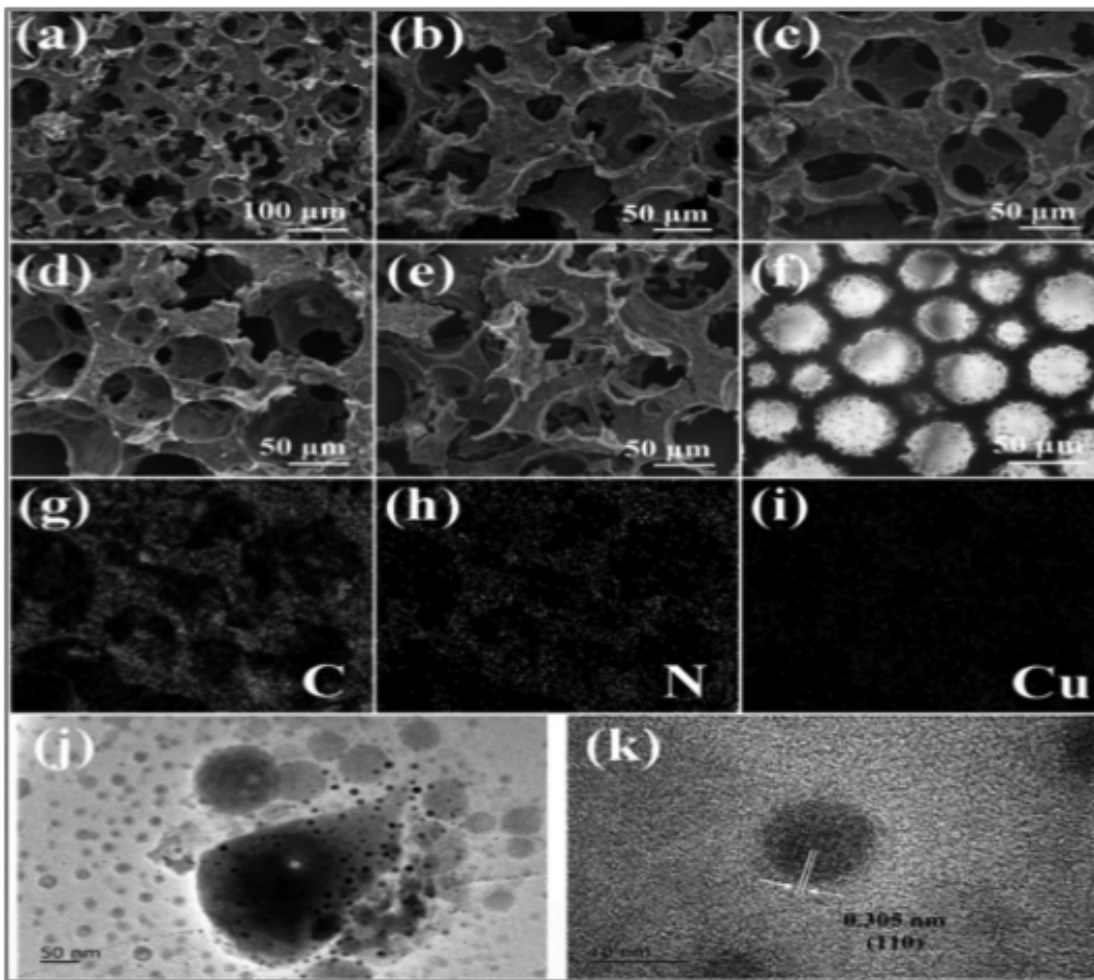


Figure 9. SEM images of pure  $\text{g-C}_3\text{N}_4$  foam (a); CFC-0.05 (b); CFC-0.1 (c); CFC-0.2 (d) and CFC-0.4 (e); (f) Optical microscope image of the  $\text{g-C}_3\text{N}_4$  foam slurry; EDX mapping spectrum of CFC-0.2 (g-i); TEM (j) and HRTEM (k) images of CFC-0.2.

$\text{N}_2$  adsorption/desorption isotherms are tested to analyze pore structure and distribution of the obtained samples, as shown in **Figure 10**. Evidently, isotherms reveal type IV and H3 hysteresis loop, corresponds to mesoporous structure of the samples, BET surface area (SBET) of pure  $\text{g-C}_3\text{N}_4$  was  $5 \text{ m}^2/\text{g}$ , increased to  $10 \text{ m}^2/\text{g}$  due to 2D nanosheets of pCN. A further increased in BET surface area of  $11 \text{ m}^2/\text{g}$  was obtained with 3% Cu-loading pCN sample, as shown in Figure 10 (a). The  $\text{N}_2$  sorption isotherm curves of  $\text{g-C}_3\text{N}_4$  foam and CFC-0.2 composite are shown in Figure 10 (b), the adsorption isotherms of all composite samples pertain to type IV isotherm, reûlecting the mesopores nature of the materials. The speciûc surface areas of  $\text{g-C}_3\text{N}_4$  foam and CFC-0.2 obtained by the Brunauer-Emmett-Teller (BET) method are  $18.974$  and  $23.271 \text{ m}^2 \cdot \text{g}^{-1}$ , respectively.

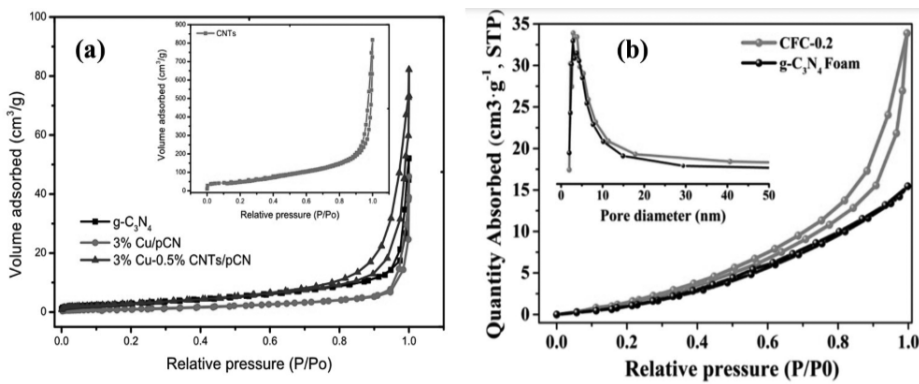


Figure 10.  $\text{N}_2$  adsorption/desorption curves and pore size distribution of CNTs,  $\text{g-C}_3\text{N}_4$  and Cu/CNTs modified pCN samples,  $\text{g-C}_3\text{N}_4$  foam and CFC-0.2.

The optical absorption spectra of as-prepared pCN and Cu/CNTs modified pCN samples,  $\text{g-C}_3\text{N}_4$  foam and all  $\text{g-C}_3\text{N}_4$  foam/ $\text{Cu}_2\text{O}$  QDs composites were recorded using UV-vis diffuse reflectance spectroscopy (UV-vis DRS). All of UV-vis DRS results presented in Figure 11. The curve of pure pCN shows light absorbance wavelength at wavelength of 470nm, attributed to band gap of 2.65 eV, as shown in Figure 11 (a). Cu-modified pCN sample has much similar spectrum which exhibits band gap energy of 2.63 eV. However, a significant light absorption towards visible region was observed in Cu-modified CNTs/ pCN sample, with absorption wavelength of 483 nm, attributed to band gap of 2.57 eV.

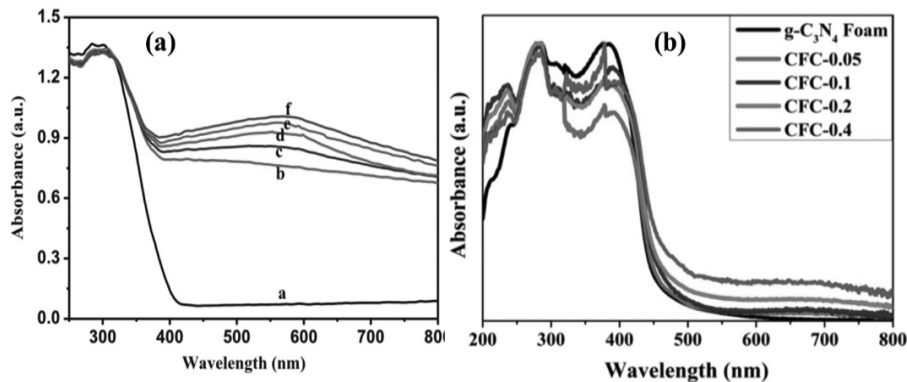


Figure 11. UV-visible analysis of pCN and Cu/CNTs modified pCN samples,  $\text{g-C}_3\text{N}_4$  foam, CFC-0.05, CFC-0.1, CFC-0.2 and CFC-0.4.

The  $\text{g-C}_3\text{N}_4$  foam possesses an absorption edge of about 450nm, while for the  $\text{g-C}_3\text{N}_4$  foam/ $\text{Cu}_2\text{O}$  QDs composites, a distinct red-shift with the absorption edge value of about 470nm can be easily discovered, as shown in Figure 11 (b). The calculated band-energy ( $E_g$ ) of  $\text{g-C}_3\text{N}_4$  foam, CFC-0.05, CFC-0.1, CFC-0.2 and CFC-0.4 samples were 2.64, 2.59, 2.56, 2.52 and 2.46 eV, respectively. Additionally, the absorption intensity of  $\text{g-C}_3\text{N}_4$  foam/ $\text{Cu}_2\text{O}$  QDs composites were enhanced in the visible region with increasing  $\text{Cu}_2\text{O}$  QDs content, indicating the absorption of the loaded  $\text{Cu}_2\text{O}$  QDs.

In order to explain how the interfacial charge transfer among synthesized nanocomposite leads to the remarkable photocatalytic performance of the  $\text{g-C}_3\text{N}_4$  foam/ $\text{Cu}_2\text{O}$  nanocomposite and  $\text{g-C}_3\text{N}_4$  foam/ $\text{Cu}_2\text{O}$  QDs, PL spectral studies were conducted. The intensity of the PL emission peak is positively correlated with the recombination probability of the photoexcited charge carriers. The PL spectra of  $\text{g-C}_3\text{N}_4$ , CNTs/pCN, Cu/ pCN, Cu-CNTs/pCN were obtained under 325nm excitation wavelength and the results are presented in Figure 12(a). All the catalysts exhibit similar trends and  $\text{g-C}_3\text{N}_4$  emission peak is the highest compared to the others, implies rapid recombination of the photoelectrons and holes in pure  $\text{g-C}_3\text{N}_4$ . However, an obvious quenching was observed in CNTs/pCN sample. This was obviously due to excellent thermal and electrical characteristics of carbon nanotubes, effective acceptor to trap the electrons, thus prevents recombination of electron and holes. The PL spectra of all samples is 370 nm, all samples present the strong PL intensity with the peak center of 458nm. The PL intensity of all composite samples was lower than that of the original  $\text{g-C}_3\text{N}_4$  foam sample, and the PL intensity decreases with the CFC-0.2 lowest. Meanwhile, series of PL spectrums were carried out with different excitation wavelength and the CFC-0.2 showed the lowest fluorescence intensity as expected, as shown in Figure 12 (b). These results indicated an efficient charge transfer pathway can effectively weaken the recombination of photogenerated  $e^- - h^+$  pairs.

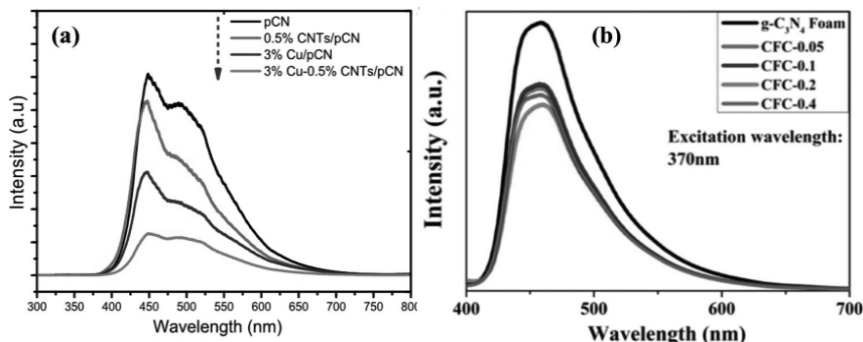


Figure 12. PL analysis of pCN and Cu/CNTs modified pCN samples,  $\text{g-C}_3\text{N}_4$ , 3% Cu/pCN, 0.5% CNTs/pCN samples and 3% Cu-0.5% CNTs/pCN samples.

#### *Photocatalytic performance and reduction of $\text{CO}_2$*

The photocatalytic activities over  $\text{g-C}_3\text{N}_4$ , pCN and Cu/CNTs modified pCN samples,  $\text{g-C}_3\text{N}_4$  powder,  $\text{g-C}_3\text{N}_4$  foam and CFC-0.2 for  $\text{CO}_2$  reduction was evaluated with reference to binary and pure catalysts, under visible light ( $\lambda > 400$ ) using high purity  $\text{CO}_2$  and water vapor. Figure 13 expresses the schematic representation of the total production of CO and  $\text{CH}_4$  in the time condition. CO and  $\text{CH}_4$  were the main products with small quantity of  $\text{CH}_3\text{OH}$  and  $\text{C}_2\text{H}_6$ . The CO of 62 imole gcat<sup>-1</sup>h<sup>-1</sup> was produced over pristine  $\text{g-C}_3\text{N}_4$ , increased to 148 imole g-cat<sup>-1</sup>h<sup>-1</sup> using pCN. The production of  $\text{CH}_4$  and  $\text{CH}_3\text{OH}$  have similar trends over pure  $\text{g-C}_3\text{N}_4$  and pCN under the same operating conditions. The CNTs/pCN heterojunction composite reveals further improvement in  $\text{CO}_2$  reduction efficiency. Highest CO evolution of 410 imole gcat<sup>-1</sup>h<sup>-1</sup> over CNTs/pCN was obtained, a 2.8-fold higher than pCN and 6.6 folds higher using pure  $\text{g-C}_3\text{N}_4$ . Similarly, amount of  $\text{CH}_4$  production was 1.15 and 1.52 folds higher than pCN and  $\text{g-C}_3\text{N}_4$  samples, respectively. This was obviously due to larger BET surface area, excellent thermal and electrical characteristics of

carbon nanotubes, effective acceptor to trap the electrons, thus prevents recombination of electron and holes, resulting in enhanced photo-activity. In order to investigate performance of CNTs/Cu loaded pCN samples, a correlation between BET surface area and CO/CH<sub>4</sub> products was established to understand prominent contributor factor in CO<sub>2</sub> reduction process as presented in Figure 13 (b). the BET surface area of Cu/pCN is closer to pCN but its CO productivity efficiency is 3.10-fold higher than using pure pCN. Similarly, BET surface area of CNTs/pCN is higher than Cu/pCN but CO production was lower than Cu/pCN. The production of CO and CH<sub>4</sub> over different types of photo-catalysts in a continuous flow fixed bed photoreactor under UV light irradiation. Using pure g-C<sub>3</sub>N<sub>4</sub>, CO production was in smaller amount, which was greatly improved in Cu and CNTs modified pCN samples as shown in Figure 13 (c). The highest amount of CO of 343 μmole/g-cat<sup>-1</sup> over 3% Cu-0.5% CNTs/pCN was obtained. Figure 13 (d) express the performance of Cu-CNTs/pCN to produce CO, CH<sub>4</sub> and CH<sub>3</sub>OH during CO<sub>2</sub> reduction with H<sub>2</sub>O under both types of irradiation (UV and visible light) has been discussed. The synthesized photo-catalyst has significantly higher productivity under solar energy than using UV-light irradiations. UV-light has higher light intensity (150mWcm<sup>-2</sup>) than visible light (100mWcm<sup>-2</sup>) but production of both CO and CH<sub>4</sub> were higher under visible light irradiations. This reveals that performance of photo-catalysts could not be enhanced by increasing light intensity, but absorption of light spectrum is also important for producing charge carriers during CO<sub>2</sub> reduction process.

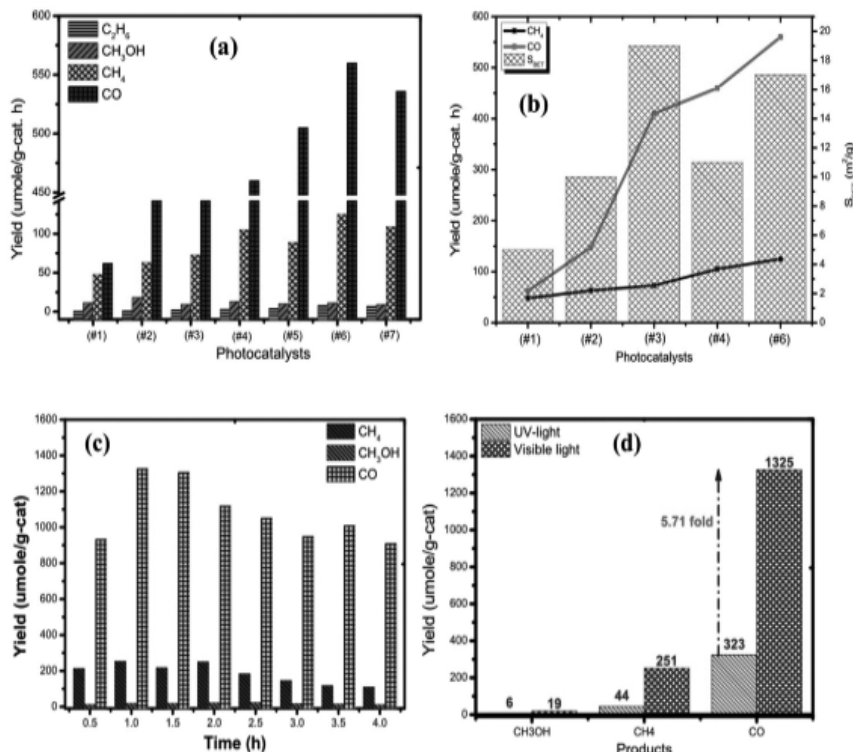


Figure 13. (a) Photocatalytic CO<sub>2</sub> reduction with H<sub>2</sub>O over different catalysts under visible light irradiations, (b) Plots of BET surface area and production rates over different catalysts (c) Effect of irradiation time on the photo-activity of 3% Cu-0.5% CNTs/ pCN catalyst for photocatalytic CO<sub>2</sub> reduction with H<sub>2</sub>O under visible light in a fixed bed reactor, (d) under the different light irradiation.

**Figure 14** presents the photocatalytic performance of as-synthesized and TiO<sub>2</sub> P25 powder (taken as a reference) at 5°C under “0.07 Mpa. CO was found to be the main carbon-based product of CO<sub>2</sub> reduction in this case. In the first hour of the reaction, all samples exhibited limited photocatalytic performance, which may be caused by the incomplete dispersing of product molecule under a large reactor space and mixed gas system, as shown in Figure 14 (a). As can be seen in Figure 14 (b) CO yield of g-C<sub>3</sub>N<sub>4</sub> powder and P25 were 0.742 μmol·g<sup>-1</sup>·h<sup>-1</sup> and 1.946 μmol·g<sup>-1</sup>·h<sup>-1</sup>, while g-C<sub>3</sub>N<sub>4</sub> foam showed the average CO production rate of 2.092 μmol·g<sup>-1</sup>·h<sup>-1</sup>.

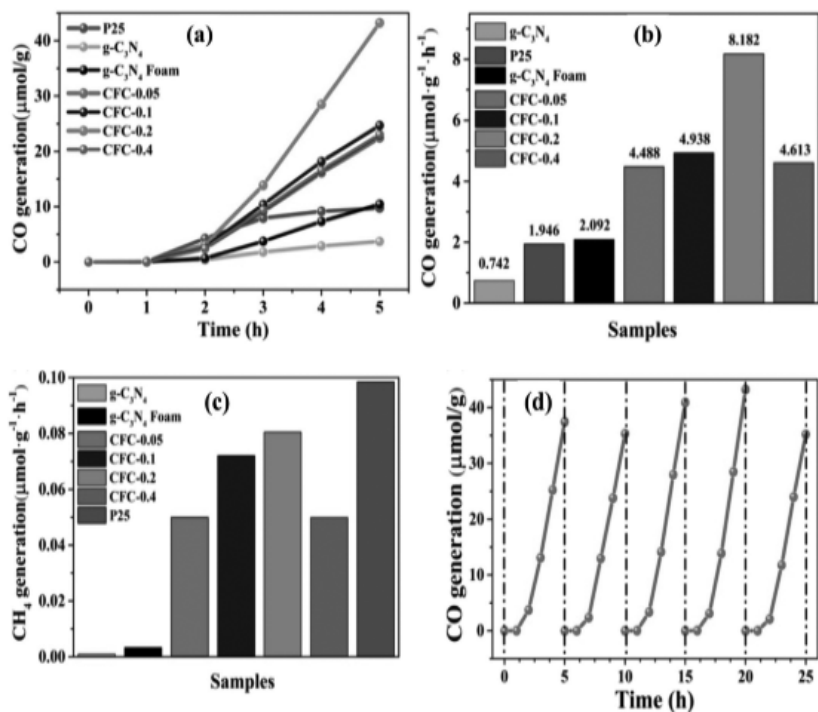
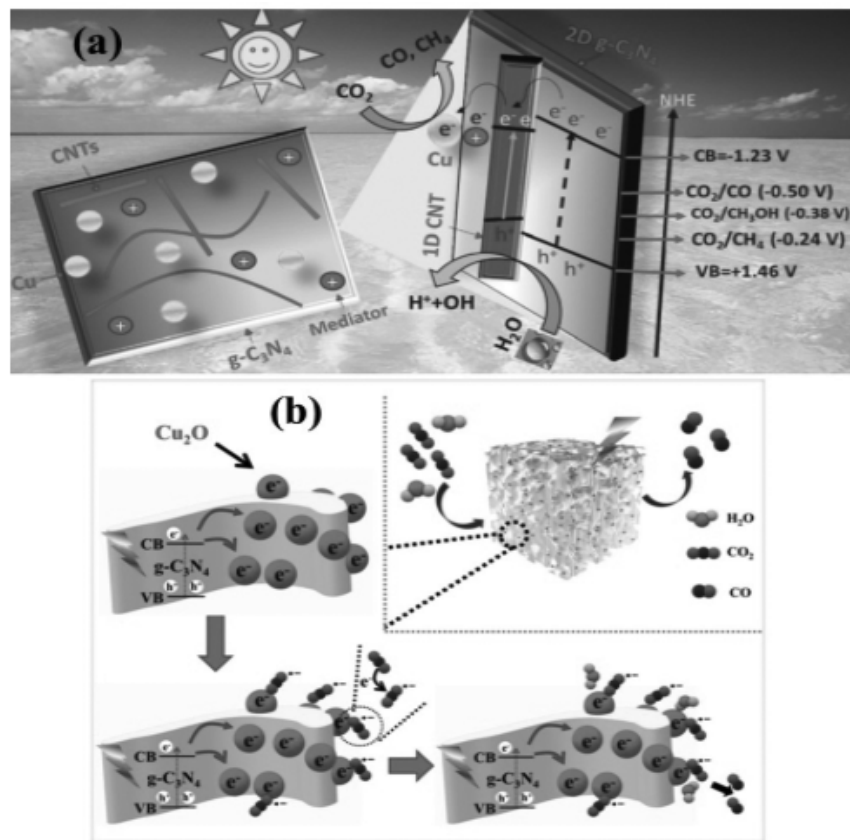


Figure 14. (a) Time courses of photocatalytic CO evolutions; average CO (b) and CH<sub>4</sub> (c) production rates of P25, bulk g-C<sub>3</sub>N<sub>4</sub>, g-C<sub>3</sub>N<sub>4</sub> foam, CFC-0.05, CFC-0.1, CFC-0.2 and CFC-0.4; (d) stability test of CO production for CFC-0.2.

The photocatalytic activity of the CFC composites was greatly improved compared to pure g-C<sub>3</sub>N<sub>4</sub> foam. The CFC-0.2 exhibited maximal photocatalytic CO evolution activity with a rate of 8.182 μmol·g<sup>-1</sup>·h<sup>-1</sup>, which is about 3.9 times higher than that of g-C<sub>3</sub>N<sub>4</sub> foam. Throughout the photocatalysis process, small amount of CH<sub>4</sub> can be detected (Figure 14 c). The CFC-0.2 also displayed optimal CH<sub>4</sub> evolution efficiency with a rate of 0.0805 μmol·g<sup>-1</sup>·h<sup>-1</sup>. The introduction of Cu<sub>2</sub>O QDs greatly increased the production of CH<sub>4</sub> simultaneously. The photocatalytic activity decreased when the Cu<sub>2</sub>O QDs amount further increased, suggesting that more Cu<sub>2</sub>O QDs loading may induce the agglomeration and then increase the whole resistance for carriers migration. The photocatalytic stability of CFC-0.2 was evaluated by collecting and reusing for five times, the photocatalytic activity of CFC-0.2 exhibited superior stability with no significant decrease after five continuous cycles as shown in Figure 14 (d). In summary, according to the structural

and performance difference before and after circle, the fluctuation of the photocatalytic activity of CFC composite may be attributed to the structural damage of  $\text{g-C}_3\text{N}_4$  foam and the agglomeration and growth of the  $\text{Cu}_2\text{O}$  QDs.



Scheme 2. Schematic illustration of the photocatalytic reduction of  $\text{CO}_2$  mechanisms of (a) Cu-CNTs/pCN, (b)  $\text{g-C}_3\text{N}_4$  foam/Cu<sub>2</sub>O QDs.

**Scheme 2** presents the schematic diagram of carbon dioxide reduction when using as-synthesized all samples under the light irradiation. Scheme 2 (a) express the carbon dioxide reduction under the light irradiation for using a a-synthesized Cu-CNTs/pCN nanocomposite. When light strikes over the photo-catalyst surface, electrons ( $e^-$ ) and holes ( $h^+$ ) are produced. Using pure  $\text{g-C}_3\text{N}_4$ , photo-recombination occurs in nanoseconds where the photo-excited electrons tend to recombine with the holes which eventually reduce the yield of desired products. However, with the presence of CNTs and Cu dopants in the pCN, the photo-excited electrons would be transported towards  $\text{CO}_2$  for its reduction. Thermodynamically, electrons trapped by metal within the photo-catalyst are more feasible if the reduction potential of the metal is more positive than the  $\text{g-C}_3\text{N}_4$  conductance band. The band region (Valence band and conduction band) synthesized and conversion potential of carbon dioxide to solar fuels are the main factor of reduction process. In the case of 2 (b) express the mechanism of reduction for using a  $\text{g-C}_3\text{N}_4$

foam/Cu<sub>2</sub>O QDs nanocomposite under the visible light irradiation in time condition. CO<sub>2</sub> was diffused into the porous framework of g-C<sub>3</sub>N<sub>4</sub> foam/Cu<sub>2</sub>O QDs and formed adsorbed CO<sub>2</sub> on the surface of the samples, the adsorbed CO<sub>2</sub> was reduced to the CO<sub>2</sub><sup>-</sup> by obtaining an electron at first. Simultaneously, the first electron adsorption for the formation of the CO<sub>2</sub><sup>-</sup> is generally acknowledged as the rate determining step in the photocatalytic reduction of CO<sub>2</sub> because the first electron transfer and adsorption process requires a more negative potential compared to the following steps. Z-scheme electron-transfer path would be dominant in the g-C<sub>3</sub>N<sub>4</sub> foam/Cu<sub>2</sub>O QDs composite system, in addition, the Cu<sub>2</sub>O QDs acted as an effective electron trap, suggesting that the photo-generated electrons on the surface of g-C<sub>3</sub>N<sub>4</sub> foam were migrated directly to Cu<sub>2</sub>O QDs, which spatially hindered the recombination of photo-generated charge carriers. The synergistic effects of 1D/2D CNTs/pCN heterojunction structured photocatalyst, and the semiconductor-metal oxide nanojunctions among the g-C<sub>3</sub>N<sub>4</sub> foam/Cu<sub>2</sub>O QDs interfaces efficiently boosted the migration of photo-generated electrons during the photocatalytic process, which could allow photoelectrons to accumulate on the surface of thereby improving photocatalytic reduction of CO<sub>2</sub> performance.

### Conclusion and outlook

To conclude, reduction of carbon dioxide is the main method for solving the environmental problems and this method divided into three categories: 1. Electrochemical, 2. Photo-electrochemical, 3. Photocatalytic. The photocatalytic carbon dioxide reduction using a catalyst material, whether pure, with doping and/or support have been estimated. The conventional metal oxides catalysts, modified or un-modified, typically exhibits high activity only under the light irradiation, especially for the UV region. Principle side of photocatalytic CO<sub>2</sub> reduction like thermodynamics, mass transfer, and selectivity and reaction mechanism have been deliberated. Approach to improve the efficiency by modifying the various aspects of Graphene-based photocatalytic system have been discussed in detail. Overall, it can be concluded that Graphene with semiconductor catalysts are efficient for CO<sub>2</sub> reduction to produce solar fuels. The yield and efficiency of process have been significantly refined by recent efforts particularly through multinary and functionalized photocatalysts. Nonetheless, basal plane defects limit the electronic conductivity of graphene; photocatalytic performance can further be amplified by defects free graphene as bridge in multinary nanocomposites. Although, significant advancements have been made in theoretical basis and performance of Graphene-based semiconductor catalyst is the great for the photocatalytic carbon dioxide reduction system, it is still outlying from practical applications.

### Reference

- [1] Houston, BP Energy Outlook: Global Energy Demand to grow 30% to 2035, 2017, Australia <http://www.ogj.com/articles/2017/01/bp-energy-outlook-global-energy-demand-to-grow-30-to-2035.html>.
- [2] D. Chen, X. Zhang, A.F. Lee. Synthetic strategies to nanostructured photocatalysts for CO<sub>2</sub> reduction to solar fuels and chemicals. *J. Mater. Chem. A*, 3 (2015), pp. 14487-14516.

- [3] Q.J. Xiang, B. Cheng, J.G. Yu. Graphene-based photocatalysts for solar-fuel generation. *Angew. Chem. Int. Ed.*, 54 (2015), pp. 11350-11366.
- [4] E.V. Kondratenko, G. Mul, J. Baltrusaitis, G.O. Larrazábal, J. Pérez-Ramírez, Status and perspectives of CO<sub>2</sub> conversion into fuels and chemicals by catalytic, photocatalytic and electrocatalytic processes. *Energy Environ. Sci.*, 6 (2013), pp. 3112-3135.
- [5] L. Yuan, Y.J. Xu. Photocatalytic conversion of CO<sub>2</sub> into value-added and renewable fuels. *Appl. Surf. Sci.*, 342 (2015), pp. 154-167.
- [6] IHSMarkit, 2017, <http://www.methanol.org/the-methanol-industry/>.
- [7] IHSMarkit, 2017, <http://news.ihsmarkit.com/press-release/country-industry-forecasting-media/global-methanol-demand-growth-driven-methanol-olefi>.
- [8] L. Tan, S.P. Chai, A.R. Mohamed, Synthesis and applications of graphene-based TiO<sub>2</sub> photocatalysts, *Chem. Sus. Chem.*, (2012)5 1868.
- [9] A. Nozik, Photoelectrolysis of water using semiconducting TiO<sub>2</sub> crystals. *Nature*, (1975) 257383.
- [10] A. Fujishima, K. Honda, Electrochemical Photolysis of Water at the semiconductor Electrode, *Nature*, (1972) 238 37.
- [11] Tahir, M., Tahir, B., Amin, N.A.S., Alias, H., Selective photocatalytic reduction of CO<sub>2</sub> by H<sub>2</sub>O/H<sub>2</sub> to CH<sub>4</sub> and CH<sub>3</sub>OH over Cu-promoted In<sub>2</sub>O<sub>3</sub>/TiO<sub>2</sub> nanocatalyst, *Appl. Surf. Sci.* 389 (2016), 46-55.
- [12] Qi, K., Cheng, B., Yu, J., Ho, W. A review on TiO<sub>2</sub>-based Z-scheme photocatalysts, *Chin. J. Catal.* 38 (2017), 1936-1955.
- [13] Tan, L.L., Ong, W.J., Chai, S.P., Mohamed, A.R. Photocatalytic reduction of CO<sub>2</sub> with H<sub>2</sub>O over graphene oxide-supported oxygen-rich TiO<sub>2</sub> hybrid photocatalyst under visible light irradiation: process and kinetic studies, *Chem. Eng. J.* 308 (2016), 248-255.
- [14] Xu, Q., Yu, J., Zhang, J., Zhang, J., Liu, G. Cubic anatase TiO<sub>2</sub> nanocrystals with enhanced photocatalytic CO<sub>2</sub> reduction activity, *Chem. Commun.* 51 (2015), 7950-7953.
- [15] Kar, P., Farsinezhad, S., Mahdi, N., Zhang, Y., Obuekwe, U., Sharma, H., Shen, J., Semagina, N., Shankar, K. Enhanced CH<sub>4</sub> yield by photocatalytic CO<sub>2</sub> reduction using TiO<sub>2</sub> nanotube arrays grafted with Au, Ru, and ZnPd nanoparticles, *Nano Res.* 9 (2016), 3478-3493.
- [16] Ola, M.M., Maroto-Valer. Synthesis, characterization and visible light photocatalytic activity of metal based TiO<sub>2</sub> monoliths for CO<sub>2</sub> reduction, *Chem. Eng. J.* 283 (2016), 1244-1253.
- [17] Tahir, M., B. Tahir, B., Amin, N.A.S., Zakaria, Z.Y. Photo-induced reduction of CO<sub>2</sub> to CO with hydrogen over plasmonic Ag-NPs/TiO<sub>2</sub> NWs core/shell hetero-junction under UV and visible light, *J. CO<sub>2</sub> Util.* 18 (2017), 250-260.
- [18] Umezawa, N., Kristoffersen, H.H., Vilhelmsen, L.B., Hammer, B. Reduction of CO<sub>2</sub> with water on Pt-loaded rutile TiO<sub>2</sub> (110) modeled with density functional theory, *J. Phys. Chem. C.* 120 (2016), 9160-9164.
- [19] Wang, Q., Dong, P., Huang, Z., Zhang, X. Synthesis of Ag or Pt nanoparticle-deposited TiO<sub>2</sub> nanorods for the highly efficient photoreduction of CO<sub>2</sub> to CH<sub>4</sub>, *Chem. Phys. Lett.* 639 (2015), 11-16.
- [20] Wang, W., Xu, D., Cheng, B., Yu, J., Jiang, C. Hybrid carbon@TiO<sub>2</sub> hollow spheres with enhanced photocatalytic CO<sub>2</sub> reduction activity, *J. Mater. Chem. A.* 5 (2017), 5020-5029.
- [21] Akple, M.S., Low, J., Liu, S., Cheng, B., Yu, J., Ho, W. Fabrication and enhanced CO<sub>2</sub> reduction performance of N-self-doped TiO<sub>2</sub> micro sheet photocatalyst by bi-cocatalyst modification, *J. CO<sub>2</sub> Util.* 16 (2016), 442-449.
- [22] Trevisan, V., Olivo, A., Pinna, F., Signoretto, M., Vindigni, F., Cerrato, G., Bianchi, C.L. C-N/TiO<sub>2</sub> photocatalysts: effect of co-doping on the catalytic performance under visible light, *Appl. Catal. B.* 160 (2014), 152-160.
- [23] Akple, M.S., Low, J., Qin, Z., Wageh, S., Al-Ghamdi, A.A., Yu, J., Liu, S. Nitrogen-doped TiO<sub>2</sub> micro sheets with enhanced visible light photocatalytic activity for CO<sub>2</sub> reduction, *Chin. J. Catal.* 36 (2015),

- 2127-2134.
- [24] Regan, B.O., Xiaoe, L., Ghaddar, T. Dye adsorption, desorption, and distribution in mesoporous TiO<sub>2</sub> films and its effects on recombination losses in dye sensitized solar cells, *Energy Environ. Sci.* 5 (2012), 7203-7215.
- [25] Wang, M., Bai, J., Le Formal, F., Moon, S.J., Cevey-Ha, L., Humphry-Baker, R., Grätzel, C., Zakeeruddin, S.M., Grätzel, M. Solid-state dye-sensitized solar cells using ordered TiO<sub>2</sub> nanorods on transparent conductive oxide as photo anodes, *J. Phys. Chem. C.* 116 (2012), 3266-3273.
- [26] Adekoya, D.O., Tahir, M., Amin, N.A.S. g-C<sub>3</sub>N<sub>4</sub>/ (Cu/TiO<sub>2</sub>) nanocomposite for enhanced photoreduction of CO<sub>2</sub> to CH<sub>3</sub>OH and HCOOH under UV/visible light, *J.CO<sub>2</sub> Util.* 18 (2017), 261-274.
- [27] Benedetti, J.E., Bernardo, D.R., Morais, A., Bettini, J., Nogueira, A.F. Synthesis and characterization of a quaternary nanocomposite based on TiO<sub>2</sub>/CdS/rGO/Pt and its application in the photoreduction of CO<sub>2</sub> to methane under visible light, *RSC Adv.* 5 (2015), 33914-33922.
- [28] Li, Y., Zhang, W., Shen, X., Peng, P., Xiong, L., Yu, Y. Octahedral Cu<sub>2</sub>O-modified TiO<sub>2</sub> nanotube arrays for efficient photocatalytic reduction of CO<sub>2</sub>, *Chin. J. Catal.* 36 (2015), 2229-2236.
- [29] Liu, J., Cheng, B., Yu, J. A new understanding of the photocatalytic mechanism of the direct Z-scheme g-C<sub>3</sub>N<sub>4</sub>/TiO<sub>2</sub> heterostructure, *Phys. Chem. Chem. Phys.* 18 (2016), 31175-31183.
- [30] Reli, M., Huo, P., Sihor, M., Ambrozova, N., Troppova, I., Matejova, L., Lang, J., Svoboda, L., Kustrowski, P., Ritz, M., Praus, P., Koci, K. Novel TiO<sub>2</sub>/C<sub>3</sub>N<sub>4</sub> Photocatalysts for photocatalytic reduction of CO<sub>2</sub> and for photocatalytic decomposition of N<sub>2</sub>O, *J. Phys. Chem. A.* 120 (2016), 8564-8573.
- [31] Meng, A.Y., Zhu, B.C., Zhong, B., Zhang, L.Y., Cheng, B. Direct Z-scheme TiO<sub>2</sub>/CdS hierarchical photocatalyst for enhanced photocatalytic H<sub>2</sub>-production activity, *Appl. Surf. Sci.* 422 (2017), 518-527.
- [32] J.I. Pankove. Optical Processes in Semiconductors. Courier Corporation (2012).
- [33] A. Kormányos, A. Thomas, M.N. Huda, P. Sarker, J. PingLiu, N. Poudyal, C. Janáky, K. Rajeshwar. *J. Phys. Chem. C*, 120 (2016), pp. 16024-16034.
- [34] C. Janaky, D. Hursán, B. Endrődi, W. Chanmanee, D. Roy, D. Liu, N.R. de Tacconi, B.H. Dennis, K. Rajeshwar. *ACS Energy Lett.*, 1 (2016), pp. 332-338.
- [35] A. Thomas, G.F. Samu, M.N. Huda, P. Sarker, J.P. Liu, V. Nguyen, E. Wang, K.A. Schug, K. Rajeshwar. *ChemSusChem*, 8 (2015), pp. 1652-1663.
- [36] J.-L. Gong, B. Wang, G.-M. Zeng, C.-P. Yang, C.-G. Niu, Q.-Y. Niu, W. J. Zhou, Y. Liang. *J. Hazard. Mater.*, 164 (2009), pp. 1517-1522.
- [37] X. Li, J. Yu, S. Wageh, A.A. Al-Ghamdi, J. Xie. *Small*, 12 (2016), pp. 6640-6696.
- [38] Y. Cui, S.I. Kundalwal, S. Kumar, **Gas Barrier Performance of Graphene/polymer Nanocomposites**, *Pergamon* (2016), pp. 313-333.
- [39] K.S. Novoselov, A.K. Geim, S.V. Morozov, Jiang D., Zhang Y., S.V. Dubonos, I.V. Grigorieva, A.A. Firsov. Electric field effect in atomically thin carbon films. *Science*, 306 (5696) (2004), pp. 666-669.
- [40] R.S., Rong P., Yu Q. Preparations, properties and applications of graphene in functional devices: a concise review. *Ceram. Int.*, 44 (11) (2018), pp. 11940-11955.
- [41] Wang S., Sun H., Ang H.M., M.O. Tadé. Adsorptive remediation of environmental pollutants using novel graphene-based nanomaterials. *Chem. Eng. J.*, 226 (2013), pp. 336-347.
- [42] B. Aurian-Blajeni, M. A. Habib, I. Taniguchi, Bockris JOM. 1983. The study of adsorbed species during the photo assisted reduction of carbon dioxide at a p-CdTe electrode. *J. Electroanal. Chem.* 157:399-404.
- [43] K. Hirota, DA. Tryk, Yamamoto T, Hashimoto K, Okawa M, Fujishima A. 1998. Photo-electrochemical reduction of CO<sub>2</sub> in a high-pressure CO<sub>2</sub> + methanol medium at p-type semiconductor electrodes. *J. Phys. Chem. B* 102:9834-43.
- [44] R. Hinogami, T. Mori, S. Yae, Y. Nakato, 1994. Efficient photo-electrochemical reduction of carbon dioxide on a p-type silicon (p-Si) electrode modified with very small copper particles. *Chem. Lett.*

- 23:1725–28.
- [45] R. Hinogami, Y.S. Nakamura, S. Yae, Y. Nakato, 1997. Modification of semiconductor surface with ultrafine metal particles for efficient photo-electrochemical reduction of carbon dioxide. *Appl. Surface Sci.* 121/122:301–4.
- [46] Y. Ma, X. Wang, Y. Jia, X. Chen, H. Han, C. Li, **Titanium dioxide-based nanomaterials for photocatalytic fuel generations**, *Chem. Rev.*, 114 (2014), pp. 9987-10043.
- [47] V. Etacheri, R. Roshan, V. Kumar, **Mg-doped ZnO nanoparticles for efficient sunlight-driven photocatalysis**, *ACS Appl. Mater. Interfaces*, 4 (2012), pp. 2717-2725.
- [48] Gallo, M. Marelli, R. Psaro, V. Gombac, T. Montini, P. Fornasiero, R. Pievo, V.D. Santo, Bimetallic Au-Pt/TiO<sub>2</sub> photocatalysts active under UV-A and simulated sunlight for H<sub>2</sub> production from ethanol, *Green Chem.*, 14 (2012), pp. 330-333
- [49] J. Zhao, Y. Wang, Y. Li, X. Yue, C. Wang, **Phase-dependent enhancement for CO<sub>2</sub> photocatalytic reduction over CeO<sub>2</sub>/TiO<sub>2</sub> catalysts**, *Catal. Sci. Technol.*, 6 (2016), pp. 7967-7975
- [50] Y. Wang, B. Li, C. Zhang, L. Cui, S. Kang, X. Li, L. Zhou, **Ordered mesoporous CeO<sub>2</sub>-TiO<sub>2</sub> composites: highly efficient photocatalysts for the reduction of CO<sub>2</sub> with H<sub>2</sub>O under simulated solar irradiation**, *Appl. Catal., B*, 130–131 (2013), pp. 277-284
- [51] A. Iwase, S. Yoshino, T. Takayama, et al. *J. Am. Chem. Soc.*, 138 (2016), pp. 10260-10264.
- [52] G. Mahmoodi, S. Sharifnia, M. Madani, V. Vatanpour, *Sol. Energy*, 97 (2013), pp. 186-194.
- [53] K. Li, B. Peng, T. Peng, **Recent advances in heterogeneous photocatalytic CO<sub>2</sub> conversion to solar fuels** *ACS Catal.*, 6 (2016), pp. 7485-7527.
- [54] C.C. Yang, Y.-H. Yu, Bvd. Linden, J.C.S. Wu, G. Mul, **Artificial photosynthesis over crystalline TiO<sub>2</sub>-based catalysts: fact or fiction?** *J. Am. Chem. Soc.*, 132 (2010), pp. 8398-8406.
- [55] T. Yui, A. Kan, C. Saitoh, K. Koike, T. Ibusuki, O. Ishitani, **Photochemical reduction of CO<sub>2</sub> using TiO<sub>2</sub>: effects of organic adsorbates on TiO<sub>2</sub> and deposition of Pd onto TiO<sub>2</sub>**, *ACS Appl. Mater. Interfaces*, 3 (2011), pp. 2594-2600.
- [56] B. Yu, Y. Zhou, P. Li, W. Tu, P. Li, L. Tang, J. Ye, Z. Zou, **Photocatalytic reduction of CO<sub>2</sub> over Ag/TiO<sub>2</sub> nanocomposites prepared with a simple and rapid silver mirror method**, *Nanoscale*, 8 (2016), pp. 11870-11874.
- [57] J. Low, S. Qiu, D. Xu, C. Jiang, B. Cheng, **Direct evidence and enhancement of surface plasmon resonance effect on Ag-loaded TiO<sub>2</sub> nanotube arrays for photocatalytic CO<sub>2</sub> reduction**, *Appl. Surf. Sci.*, 434 (2018), pp. 423-432.
- [58] N. Singhal, A. Ali, V. Vorontsov, P. Chandrashekhar, U. Kumar, *Appl Cat A: General*, 523 (2016), pp. 107-117.
- [59] J. Yu, J. Low, W. Xiao, P. Zhou, M. Jaroniec, **Enhanced photocatalytic CO<sub>2</sub>-reduction activity of anatase TiO<sub>2</sub> by coexposed {001} and {101} facets**, *J. Am. Chem. Soc.*, 136 (2014), pp. 8839-8842.





This document was created with the Win2PDF “print to PDF” printer available at  
<http://www.win2pdf.com>

This version of Win2PDF 10 is for evaluation and non-commercial use only.

This page will not be added after purchasing Win2PDF.

<http://www.win2pdf.com/purchase/>